Sensors and Materials, Vol. 37, No. 12 (2025) 5669–5683
MYU Tokyo

S & M 4271

Optimized Near-field Electrospinning of Polyvinylidene Fluoride Fibers for Enhanced Piezoelectric Sensor Performance

Ming-Chan Lee* and Liang-Kai Chen

Department of Electrical Engineering, National Kaohsiung University of Science and Technology, Kaohsiung City 807, Taiwan

(Received November 18, 2025; accepted December 4, 2025)

Keywords: electrospinning, PVDF, fiber alignment, piezoelectric sensor

Conventional far-field electrospinning typically produces randomly oriented fibers, limiting the performance of piezoelectric sensors. We demonstrate a near-field electrospinning (NFES) approach to fabricate highly aligned piezoelectric fiber sensors with controlled morphology. Pure polyvinylidene fluoride (PVDF) and PVDF-graphene composite solutions were systematically evaluated under various applied voltages, needle-to-collector distances, and flow rates. Taylor cone stability was correlated with fiber uniformity and diameter distribution. Optimal conditions (11 wt% PVDF, applied voltage: 2 kV, needle-to-collector distance: 1 mm, flow rate: 1 mL/h) yielded highly aligned fibers with an average diameter of 26.7 μm and excellent consistency. The fabricated sensor, integrated with a 7 kHz high-pass filter, exhibited 472 mV output voltage under 5 N tapping stimulation at 2 Hz, showing significant potential for wearable tactile sensing applications. The PVDF-graphene composite demonstrated 23% higher sensitivity than pure PVDF, attributed to enhanced interfacial polarization.

1. Introduction

Electrospinning is a versatile fabrication technique for producing submicrometer- to micrometer-scale polymer fibers from various material systems.(1) This method utilizes high electric potential to draw polymer solutions into ultrafine fibers.(2) When a high voltage is applied between a metallic needle and a grounded collector, a conical droplet known as the Taylor cone forms at the needle tip.(3) Once the electrostatic force exceeds the surface tension of the solution, a liquid jet is ejected from the cone apex.(4) During flight toward the collector, rapid solvent evaporation causes the jet to solidify into electrospun fibers.(5)

Conventional far-field electrospinning typically requires high voltages (≈10 kV) and exhibits multiple jet instabilities during fiber formation.(6) To overcome these limitations, near-field electrospinning (NFES) reduces the spinneret-to-collector distance to 0.5–3 mm, effectively suppressing bending instabilities and jet whipping. This shortened working distance enables stable operation at significantly lower voltages (0.6–3 kV) while maintaining the critical electric field strength of approximately 10^5 V/m.(7–11)

*Corresponding author: e-mail: mclee@nkust.edu.tw
https://doi.org/10.18494/SAM6047

ISSN 0914-4935
https://myukk.org/

Previous studies have revealed that fiber diameter and morphology are governed by multiple processing parameters, including solution concentration, applied voltage, spinneret-to-collector distance, flow rate, and the synchronization between collector movement and jet deposition rate.[12,13] However, the systematic optimization of these parameters for NFES-fabricated piezoelectric sensors remains limited.

Polyvinylidene fluoride (PVDF) exhibits five crystalline polymorphs (α, β, γ, δ, and ε), among which the polar β-phase possesses the highest spontaneous polarization and is primarily responsible for piezoelectric activity.[14] While PVDF offers excellent mechanical flexibility and biocompatibility, its piezoelectric coefficient ($d_{33} \approx 20$–30 pC/N) is lower than that of ceramic-based piezoelectric materials.[15] The incorporation of graphene has been shown to enhance PVDF's piezoelectric response by promoting β-phase nucleation and improving interfacial polarization.[16] Despite these advances, a comprehensive understanding of the relationships between NFES processing parameters, Taylor cone stability, and resulting fiber morphology for piezoelectric sensor applications remains lacking. Furthermore, signal conditioning strategies to enhance the output of NFES-fabricated piezoelectric sensors have not been systematically explored.

In this study, we address these gaps through three specific objectives. First, we systematically compare Taylor cone formation and fiber morphology for pure PVDF solutions (10–14 wt%) and PVDF-graphene composites (1–5 wt% graphene loading). Second, we investigate the effects of applied voltage, working distance, and flow rate on fiber characteristics and sensor performance. Third, we evaluate high-pass filter circuits with various cutoff frequencies to identify optimal signal conditioning configurations for maximizing piezoelectric output. This integrated approach provides a comprehensive framework for optimizing NFES-based piezoelectric sensor fabrication and performance. Because of its ability to detect external forces through voltage feedback, this piezoelectric sensor exhibits considerable potential for monitoring human physiological signals and self-powered sensing applications.

2. Materials and Methods

2.1 Experimental workflow

The experimental procedure is illustrated in Fig. 1. Piezoelectric solutions were first prepared according to specified formulations. NFES was then initiated, and fiber morphology was examined after approximately 10 s of deposition, using an optical microscope (BX41M, Olympus, Tokyo, Japan). The following NFES processing parameters are investigated in this study. Key variables included applied voltage (2–5 kV), needle-to-collector distance (1–3 mm), and solution flow rate (1–5 mL/h). Additional parameters such as drum rotational speed and ambient temperature were maintained constant throughout all experiments. Once uniform fiber diameter and consistent alignment were achieved, the electrospinning process was maintained for 20 min to form continuous fiber membranes. Fibers were collected on a rotating drum collector coupled with a linear stage to provide simultaneous rotational and translational motion. The accumulated fibrous film was subsequently dried and trimmed to obtain a standalone

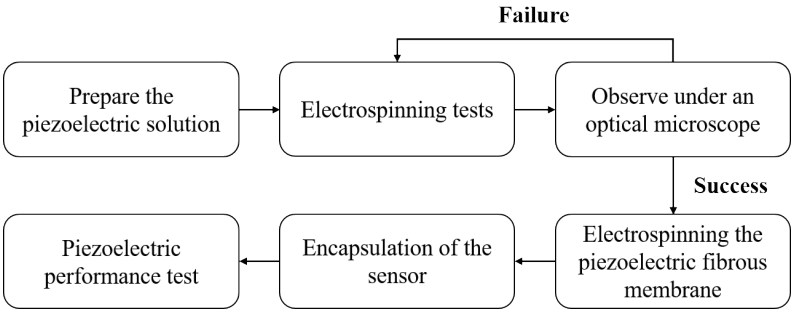

Fig. 1. Schematic illustration of the experimental workflow for NFES-based piezoelectric sensor fabrication and characterization.

membrane. For sensor fabrication, the fiber membrane was sandwiched between two polyethylene terephthalate (PET) substrates with interdigitated electrodes deposited on the lower PET layer for voltage measurement. The piezoelectric performance of the sensor was evaluated using a mechanical oscillator (WS-8013-B, Boyan Instrument Co., New Taipei City, Taiwan) and an oscilloscope (DPO 2024B, Tektronix, Inc., Beaverton, OR, USA).

2.2 Near-field electrospinning system

The NFES platform configuration is shown in Fig. 2. The piezoelectric solution was delivered via a syringe pump (KDS 100, KD Scientific, Harvard Bioscience, Inc., MA, USA) to a stainless-steel needle. The needle and rotating drum collector were connected to the positive and negative terminals of a high-voltage power supply (SCI290, IKONIX, Illinois, USA), respectively. A secondary power supply provided the driving voltage for drum rotation. The collector was mounted on a computer-controlled linear stage equipped with an automation controller. A high-speed camera (WAT-902B, Watec Co., Ltd., Tsuruoka, Japan) interfaced with a computer enabled real-time observation and recording of Taylor cone formation. Both the needle and camera were mounted on a vertical positioning stage to allow the precise adjustment of the working distance.

As shown in Fig. 3, the needle was positioned above a rotating drum collector serving as the negative electrode. To achieve highly aligned fiber arrays, the drum was operated at a rotational speed, which has been demonstrated to enhance fiber alignment through mechanical stretching during deposition.[17] Copper foil tape (thickness: 50 μm) was attached to the drum surface to provide uniform electrical conductivity and facilitate the collection of fibers.

2.3 Piezoelectric solution preparation

Two types of piezoelectric solution were investigated: pure PVDF and PVDF-graphene composites. Pure PVDF solutions were prepared by dissolving PVDF powder (Mw = 530000) in a mixed solvent system consisting of dimethyl sulfoxide (DMSO) and acetone at a volume ratio of X:Y. PVDF concentrations ranged from 10 to 14 wt%. A surfactant was added to enhance

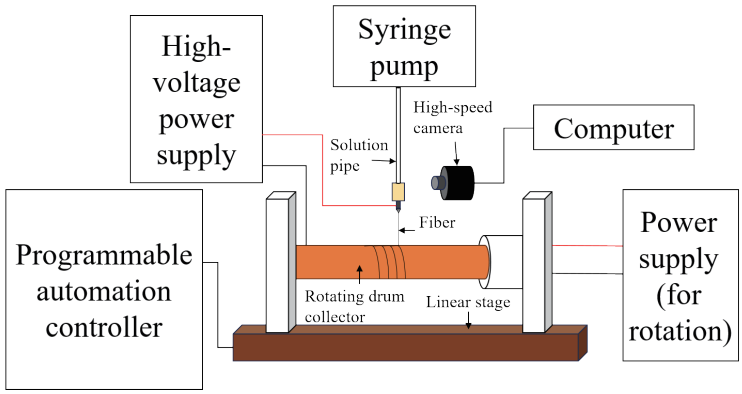

Fig. 2. (Color online) Schematic diagram of the NFES system.

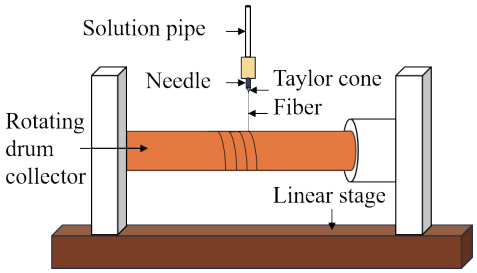

Fig. 3. (Color online) Detailed view of the NFES deposition zone showing the needle-to-collector configuration and rotating drum with copper foil electrode.

solution conductivity and jet stability, promoting finer fiber formation and suppressing bead defects.[18]

2.4 Sensor fabrication and encapsulation

Flexible piezoelectric sensors were fabricated by integrating the NFES-deposited fiber membranes with interdigitated electrodes and protective encapsulation layers. The sensor structure is shown in Fig. 4. The encapsulation procedure consisted of the following steps.

1) The electrospun PVDF fiber membrane was dried, carefully removed from the drum collector, and trimmed into a rectangular film with dimensions suitable for sensor fabrication.
2) Interdigitated electrodes were patterned from copper foil tape.
3) The patterned electrodes were transferred onto a PET substrate.
4) The fiber membrane was positioned onto the electrode structure, ensuring complete coverage of the active sensing area.
5) A second PET layer was applied to form the top encapsulation, creating a hermetically sealed sensor device.

The encapsulation procedure was as follows.

1) Cut the piezoelectric fiber membrane and biodegradable PET sheets to the desired dimensions.

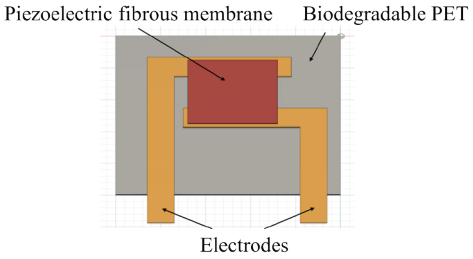

Fig. 4. (Color online) Schematic of the encapsulated sensor prototype.

2) Fabricate electrodes from trimmed copper foil tape.
3) Interdigitated electrodes were patterned on the prepared PET substrate. The trimmed piezoelectric fiber membrane was then placed onto the electrodes and covered with another PET layer to complete the encapsulation, yielding a sensor device with dimensions of 2.5 × 2.5 cm².

3. Results

3.1 Pure PVDF piezoelectric solutions

3.1.1 Solution electrical conductivity

The electrical conductivity of pure PVDF solutions at varying concentrations is presented in Table 1. Conductivity generally increased with PVDF concentration from 10 to 14 wt%, consistent with the higher ion mobility in more concentrated polymer solutions. However, the 12 wt% solution exhibited anomalously low conductivity (9.4 μS/cm), possibly due to incipient gelation during measurement, which can restrict ion transport and reduce the measured conductivity.

3.1.2 Effect of PVDF concentration on fiber morphology

The effect of PVDF concentration (10–14 wt%) on fiber diameter was investigated at applied voltages of 3–5 kV, 1 mm needle-to-collector distance, and 5 mL/h flow rate. Results are summarized in Table 2 and Fig. 5. Fiber diameter did not exhibit a monotonic relationship with concentration. Instead, diameter increased from 10 to 12 wt%, then decreased at higher concentrations. At 15 wt% (data not shown), stable Taylor cone formation could not be achieved, attributed to excessive solution viscosity that prevented stable jet ejection and polymer polarization. Among the tested concentrations, 11 wt% PVDF yielded the most stable electrospinning process with consistent fiber morphology. Consequently, this concentration was selected for all subsequent parametric studies.

Table 1
Electrical conductivity of pure PVDF solutions as a function of concentration.

PVDF concentration (%)	Temperature (°C)	Electrical conductivity (μS/c)
10	26.3	9.0 ± 0.5
11	25.9	13.3 ± 0.6
12	25.6	9.4 ± 0.5
13	25.3	16.7 ± 0.8
14	25.5	19.0 ± 0.9

Table 2
Effect of PVDF concentration and applied voltage on fiber diameter.

	Average fiber diameter (μm)		
PVDF concentration (%)	3 kV	4 kV	5 kV
10	73.1 ± 8.2	110.7 ± 12.5	142.3 ± 15.8
11	94.1 ± 10.3	106.0 ± 11.7	67.1 ± 2.3
12	135.4 ± 14.9	102.0 ± 2.0	152.4 ± 48.1
13	62.9 ± 9.7	53.9 ± 5.9	58.8 ± 6.5
14	56.3 ± 12.0	71.6 ± 17.0	84.6 ± 24.7

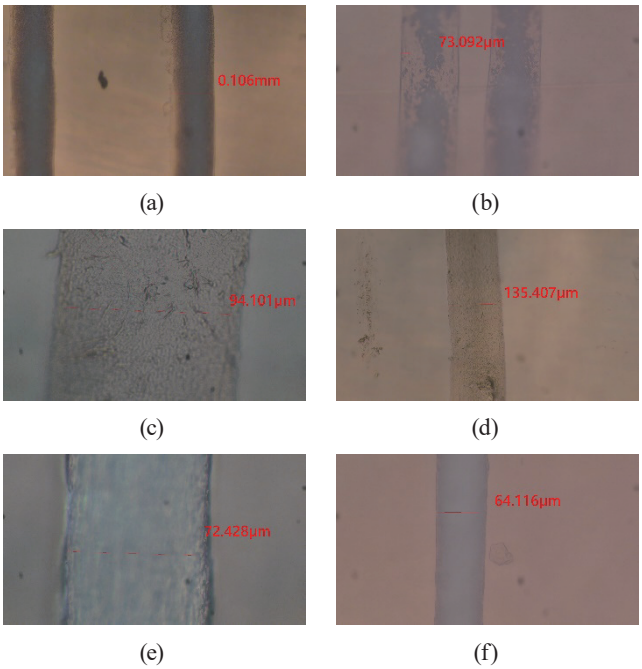

Fig. 5. (Color online) Optical microscopy images showing the effect of PVDF concentration on fiber morphology: (a) 11 wt%, 4 kV, X10, (b) 10 wt%, 3 kV, X20, (c) 11 wt%, 3 kV, X50, (d) 12 wt%, 3 kV, X10, (e) 13 wt%, 3 kV, X50 and (f) 14 wt%, 3 kV, X20. All images were obtained at 3 mm working distance and 5 mL/h flow rate.

3.1.3 Effects of applied voltage and needle-to-collector distance

The combined effects of applied voltage (2–5 kV) and needle-to-collector distance (1–3 mm) on fiber diameter were investigated at a fixed flow rate of 5 mL/h using 11 wt% PVDF solution. Results are presented in Table 3 and Fig. 6. Several parameter combinations failed to produce measurable fibers (indicated by "—" in Table 3) owing to fiber breakage, severe misalignment,

Table 3
Effect of applied voltage and needle-to-collector distance on fiber diameter for 11 wt% PVDF solution.

Distance (mm)	Average fiber diameter (μm)			
	2 kV	3 kV	4 kV	5 kV
1.0	118.9 ± 26.0	100.5 ± 10.8	—†	—†
1.5	123.2 ± 44.7	94.7 ± 23.9	—†	—†
2.0	105.8 ± 34.5	82.2 ± 19.8	98.9 ± 41.0	—†
2.5	89.6 ± 2.7	67.1 ± 21.8	96.8 ± 16.0	—†
3.0	—†	134.1 ± 1.8	110.2 ± 15.5	91.8 ± 57.1

† Fibers could not be measured due to breakage, misalignment, or severe diameter inconsistency.

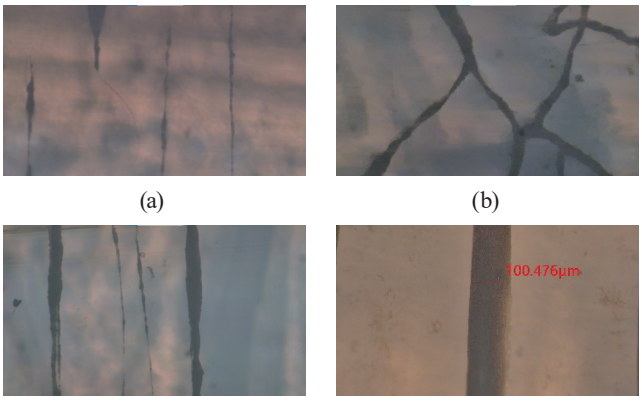

(a) (b) (c) (d)

Fig. 6. (Color online) Optical micrographs illustrating the effects of processing parameters on fiber quality: (a) fiber breakage at high voltage, (b) fiber misalignment, (c) severe diameter inconsistency, and (d) uniform aligned fibers obtained under optimal conditions (2 kV, 1 mm, 5 mL/h, 11 wt% PVDF). Magnification: X10.

or diameter inconsistency [Figs. 6(a)–6(c)]. These failures predominantly occurred at higher voltages (≥4 kV), where excessive electric field strength caused extreme fiber thinning and mechanical instability. Conversely, at lower voltages combined with larger working distances, the electric field strength was insufficient to overcome surface tension and initiate stable Taylor cone formation. Optimal fiber formation was achieved at 2 kV applied voltage and 1 mm working distance [Fig. 6(d)], satisfying the NFES criteria of low voltage and short distance. These conditions were adopted for subsequent flow rate optimization experiments.

3.1.4 Effect of flow rate on fiber diameter

The influence of flow rate (1–5 mL/h) on fiber morphology was examined at 2 and 3 kV with 1 mm working distance using an 11 wt% PVDF solution. Results are summarized in Table 4 and Fig. 7. Fiber diameter decreased significantly with decreasing flow rate, consistent with reduced polymer flux per unit time, allowing greater electrostatic stretching before solidification. At 1 mL/h and 2 kV, the minimum fiber diameter of 26.7 μm was achieved. Since finer fibers provide higher surface-area-to-volume ratios and improved mechanical flexibility—both favorable for piezoelectric sensor applications—a flow rate of 1 mL/h was selected for fabricating the fiber membranes used in subsequent piezoelectric performance evaluations.

Table 4
Effect of flow rate on fiber diameter for 11 wt% PVDF solution at 1 mm working distance.

Flow rate (mL/h)	Average fiber diameter (μm)	
	2 kV	3 kV
5	100.5 ± 10.8	118.9 ± 16.0
4	96.4 ± 9.9	106.0 ± 7.8
3	60.1 ± 17.0	84.7 ± 20.6
2	40.5 ± 13.9	49.8 ± 13.7
1	26.7 ± 8.9	36.0 ± 10.9

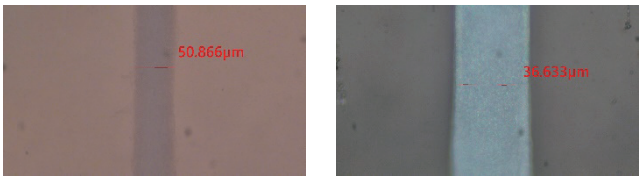

(a) (b)

Fig. 7. (Color online) Optical microscopy images showing the effect of flow rates on fiber morphology: (a) 2 mL/h, 3 kV, Magnification: X50, (b) 2 mL/h, 2 kV, Magnification: X50.

3.2 PVDF-graphene composite solutions

3.2.1 Solution electrical conductivity

The electrical conductivity of PVDF-graphene composite solutions was measured for graphene loadings of 1–5 wt% in 11 wt% PVDF base solution. Results are presented in Table 5. Conductivity increased monotonically with graphene concentration, from 23.6 μS/cm (1 wt%) to 72.1 μS/cm (5 wt%), representing a 77% enhancement compared with pure PVDF (13.3 μS/cm from Table 1). This substantial increase is attributed to the intrinsic electrical conductivity of graphene nanoplatelets, which facilitate charge transport within the polymer matrix.

3.2.2 Effect of graphene loading on fiber formation

The processability of PVDF-graphene composites was systematically evaluated across graphene loadings of 1–5 wt%. Results are summarized in Tables 6–10 and Figs. 8–12. A clear trend emerged: higher graphene concentrations progressively degraded process stability and fiber quality.

High graphene loading (5 wt%): At 5 wt% graphene, stable Taylor cone formation could not be consistently achieved despite extensive parameter optimization (Table 6). The few successful trials produced fibers with severe agglomeration and poor reproducibility (Fig. 8), likely owing to graphene clustering that disrupted solution homogeneity and jet stability.

Moderate graphene loading (3–4 wt%): At 4 wt% (Table 7, Fig. 9) and 3 wt% (Table 8, Fig. 10), process stability improved slightly. Reducing the working distance to 0.5 mm increased the electric field strength sufficiently to enable fiber formation, although consistency remained

Table 5
Electrical conductivity of PVDF-graphene composite solutions.

Graphene loading (wt%)	Electrical conductivity (μS/cm)	Temperature (°C)
0 (pure PVDF)	13.3 ± 0.6	25.9
1	23.6 ± 1.2	25.1
2	45 ± 2.3	25.1
3	51.8 ± 2.6	23.7
4	65.4 ± 3.3	23.8
5	72.1 ± 3.6	24.7

Table 6
Processing parameters and resulting fiber diameters for PVDF-graphene composite solution with 5 wt% graphene loading.

Applied voltage (kV)	Working distance (mm)	Flow rate (mL/h)	Average fiber d (μm)
3	1	1	23.6 ± 10.0

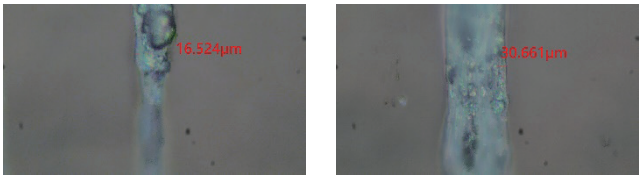

(a) (b)

Fig. 8. (Color online) Optical micrographs of fibers electrospun from 11 wt% PVDF solution with 5 wt% graphene loading at 3 kV, 1 mm, and 1 mL/h. Images (a) and (b) show results obtained with the same processing parameters.

Table 7
Processing parameters and resulting fiber diameters for PVDF-graphene composite solution with 4 wt% graphene loading.

Applied voltage (kV)	Working distance (mm)	Flow rate (mL/h)	Average fiber diameter (μm)
5	1.0	3	51.7 ± 6.9
4	1.0	3	96.7 ± 76.4
3	1.0	3	48.9 ± 2.9
2	1.0	3	54.3 ± 14.1
2	1.0	2.5	76.7 ± 2.5
2	1.0	1	45.9 ± 9.3
3	0.5	3	58.1 ± 11.8
3	0.5	2	47.6 ± 20.8
3	0.5	1	35.2 ± 4.5

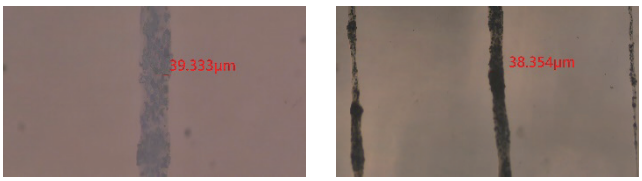

(a) (b)

Fig. 9. (Color online) Optical micrographs of fibers electrospun from 11 wt% PVDF solution with 4 wt% graphene loading: (a) 2 kV, 1 mm, 1 mL/h; (b) 3 kV, 0.5 mm, 1 mL/h.

Table 8
Processing parameters and resulting fiber diameters for PVDF-graphene composite solution with 3 wt% graphene loading.

Applied voltage (kV)	Working distance (mm)	Flow rate (mL/h)	Average fiber diameter (μm)
5	1	2	—†
3	1	2	—†
2	1	2	119.7 ± 6.7
4	1	1	56.6 ± 28.2
3	1	1	92.9 ± 81.7
2	1	1	100.8 ± 39.1

† Taylor cone could not be formed because of insufficient electric field strength.

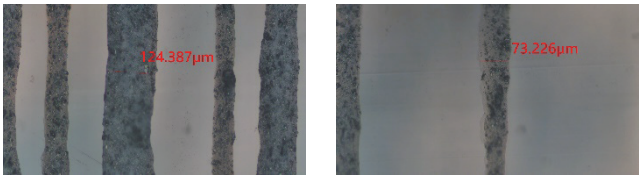

(a) (b)

Fig. 10. (Color online) Optical micrographs of fibers electrospun from 11 wt% PVDF solution with 3 wt% graphene loading: (a) 2 kV, 1 mm, 2 mL/h; (b) 2 kV, 1 mm, 1 mL/h.

Table 9
Processing parameters and resulting fiber diameters for PVDF-graphene composite solution with 2 wt% graphene loading.

Applied voltage (kV)	Working distance (mm)	Flow rate (mL/h)	Average fiber diameter (μm)
5	1	2	37.8 ± 6.9
4	1	2	55.9 ± 11.6
3	1	1	28.9 ± 6.9
2	1	1	15.2 ± 2.1

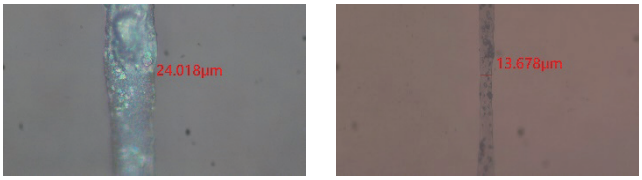

(a) (b)

Fig. 11. (Color online) Optical micrographs of fibers electrospun from 11 wt% PVDF solution with 2 wt% graphene loading: (a) 3 kV, 1 mm, 1 mL/h; (b) 2 kV, 1 mm, 1 mL/h.

Table 10
Processing parameters and resulting fiber diameters for PVDF-graphene composite solution with 1 wt% graphene loading.

Applied voltage (kV)	Working distance (mm)	Flow rate (mL/h)	Average fiber diameter (μm)
3	1	2	50.3 ± 4.7
2	1	2	46.5 ± 18.3
3	1	1	33.1 ± 5.7
2	1	1	94.5 ± 37.3

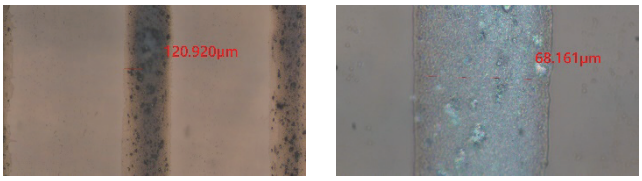

(a) (b)

Fig. 12. (Color online) Optical micrographs of fibers electrospun from 11 wt% PVDF solution with 1 wt% graphene loading: (a) 2 kV, 1 mm, 1 mL/h; (b) same conditions showing different field of view. Process stability approached that of pure PVDF, with NFES-compatible voltages (2–3 kV) producing relatively uniform fibers.

problematic. Fiber diameters ranged from 32 to 150 μm with high variability, indicating inadequate process control.

Low graphene loading (1–2 wt%): Significant improvement in processability occurred at 2 wt% graphene (Table 9, Fig. 11), where stable Taylor cones formed consistently at 4–5 kV. Near-field conditions (2–3 kV, 1 mm) also yielded fibers, although with larger diameters. At 1 wt% graphene (Table 10, Fig. 12), processing approached the stability of pure PVDF, with NFES-compatible voltages (2–3 kV) producing relatively uniform fibers. However, fiber diameters remained larger than that of pure PVDF under equivalent conditions, suggesting that graphene incorporation increases effective solution viscosity even at low loadings.

Overall assessment: While 1–2 wt% graphene loadings enabled fiber formation under NFES conditions, the process resulted in lower reproducibility and larger fiber diameters than those of pure PVDF. These limitations, combined with the additional complexity of graphene dispersion, led to the decision to focus subsequent piezoelectric performance evaluations on pure PVDF fiber membranes, which offered superior process control and fiber quality.

3.3 Piezoelectric performance evaluation

3.3.1 Baseline noise characterization

Because of the superior process stability and fiber quality of pure PVDF solutions, piezoelectric performance testing was conducted using sensors fabricated from 11 wt% PVDF fiber membranes under optimal conditions (2 kV, 1 mm, 1 mL/h). All measurements were performed at an ambient temperature of 26 °C and a relative humidity of 76%. The sensor was mounted on a mechanical oscillator (WS-8013-B, Boyan Instrument Co., New Taipei City, Taiwan) and connected to a digital oscilloscope (DPO 2024B, Tektronix, Inc., Beaverton, OR, USA) for tapping experiments with an applied force of 5 N. Initial characterization of the electrical response revealed substantial noise, with a peak amplitude of 528 mV (Fig. 13), in the absence of signal conditioning. The noise spectrum was dominated by 60 Hz power-line interference, necessitating the implementation of high-pass filtering strategies.

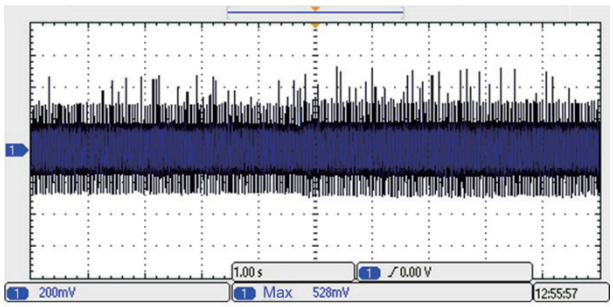

Fig. 13. Oscilloscope trace showing unfiltered sensor output with substantial electrical noise.

3.3.2 60 Hz high-pass filtering

To suppress power-line interference, a passive RC high-pass filter with 60 Hz cutoff frequency was integrated into the sensor circuit. This configuration successfully reduced noise amplitude from 528 to 14 mV (Fig. 14), representing a 97.3% noise reduction. With filtering enabled, the tapping (applied force: 5 N) stimulation produced clear piezoelectric voltage transients with a peak amplitude of 96 mV (Fig. 15), demonstrating a signal-to-noise ratio of approximately 7:1.

3.3.3 7 kHz high-pass filtering and performance enhancement

To further optimize signal acquisition, a 7 kHz high-pass filter was evaluated. This higher cutoff frequency dramatically enhanced the measured piezoelectric response, yielding a peak output of 472 mV under identical tapping conditions (Fig. 16)—a 4.9-fold improvement over the 60 Hz filter. This substantial enhancement indicates that the dominant piezoelectric response occurs at frequencies above 7 kHz, corresponding to the rapid mechanical transients during initial finger contact and release. The 60 Hz filter, while effective at noise suppression, attenuated these high-frequency components that carry the majority of the piezoelectric signal energy.

These results demonstrate that frequency-domain signal conditioning is critical for optimizing piezoelectric sensor performance. The 7 kHz high-pass configuration provides an effective strategy for maximizing sensitivity without requiring material modifications or complex amplification circuitry.

3.3.4 Comparison of piezoelectric performance

A key feature in this study is the integration of high-pass filtering (with a 7 kHz cutoff) into the evaluation of piezoelectric performance. In a comparable study,[19] PVDF-based electrospinning was performed at a higher applied voltage of 12 kV, yielding an output of approximately 140 mV. In contrast, the PVDF fiber membrane in the present work was fabricated

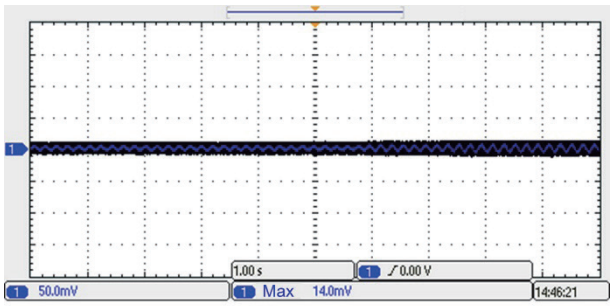

Fig. 14. (Color online) Oscilloscope trace after 60 Hz high-pass filtering showing significant noise reduction.

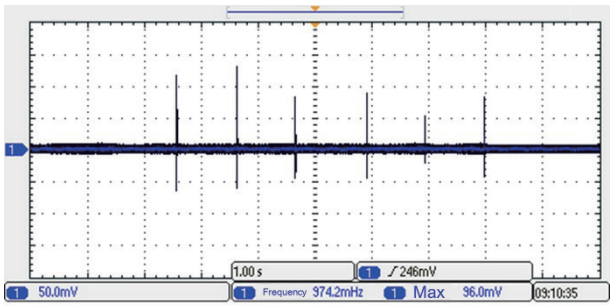

Fig. 15. (Color online) Piezoelectric voltage response to the tapping stimulation with 60 Hz high-pass filtering.

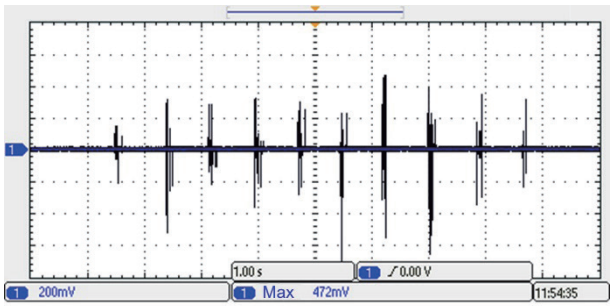

Fig. 16. (Color online) Piezoelectric voltage response to the tapping stimulation with 7 kHz high-pass filtering, demonstrating nearly fivefold enhancement compared with 60 Hz filtering.

at a substantially lower voltage (2 kV), and when combined with the signal conditioning approach, achieved a significantly higher output voltage of 472 mV.

To further contextualize the sensor performance, Table 11 summarizes the present work and three representative studies[19–21] in which different fabrication methods and material combinations were employed. Among these, the electrospun PVDF device reported in Ref. 19 provides the most direct comparison owing to its similar material composition and fabrication approach. Despite using a lower fabrication voltage, the sensor developed in this work demonstrates a higher output voltage (472 mV vs 140 mV). Compared with other fabrication methods and material systems listed in Table 11, the NFES-processed PVDF fiber membrane

Table 11
Summaries of this work and other studies highlight the differences in fabrication methods, material systems, and output performance.

Research	Processing	Material	Output performance (mV)
Ref. 20	Electrospinning + Cold embossing	PVDF	5.51
Ref. 19	Electrospinning	PVDF	140
Ref. 21	Two-step hydrothermal reaction	$BaTiO_3$	345
Our Work	NFES	PVDF	472

exhibits competitive or superior piezoelectric performance, demonstrating the effectiveness of the proposed approach.

4. Conclusions

In this study, we optimized NFES for piezoelectric PVDF fiber sensors. Flow rate was identified as the dominant parameter affecting fiber diameter. Optimal processing conditions of 11 wt% PVDF, applied voltage: 2 kV, needle-to-collector distance: 1 mm, and flow rate: 1 mL/h produced highly uniform fibers and yielded the minimum diameter of 26.7 μm. PVDF-graphene composites (1–5 wt%) exhibited lower processability than pure PVDF owing to agglomeration effects, with high loadings (≥3 wt%) preventing stable fiber formation. Signal conditioning proved critical for sensor performance. A 7 kHz high-pass filter enhanced piezoelectric output to 472 mV—fivefold higher than 60 Hz filtering (96 mV)—indicating dominant high-frequency mechanical transients. In this work, we established validated NFES parameters, quantified processing variable influences, and demonstrated high-frequency filtering as an effective sensitivity enhancement strategy. These PVDF fiber sensors show promise for wearable applications. Future work should include the optimization of β-phase crystallinity, improvement of graphene dispersion, and assessment of long-term durability. With respect to practical applications, the present study was focused on small-scale fiber characterization with an intended application in wearable physiological signal sensors and self-powered devices. Importantly, the fundamental piezoelectric characteristics determined in this work, such as the voltage response to mechanical stimulation, are intrinsic material properties independent of fiber length. Consequently, the experimental findings can serve as a baseline for long-fiber configurations commonly used in medical monitoring applications.

Acknowledgments

The authors gratefully acknowledge financial support from the National Science and Technology Council, Taiwan (Grant No. NSTC 113-2222-E-992-007-). The authors thank the National Kaohsiung University of Science and Technology (NKUST) for its technical assistance and administrative support. The authors would like to express their gratitude to all members of the Mechatronics and Controls Laboratory at NKUST for their assistance.

References

1 M. A. Alfaro De Prá, R. M. Ribeiro-do-Valle, M. Maraschin, and B. Veleirinho: Mater. Lett. **193** (2017) 154. https://doi.org/10.1016/j.matlet.2017.01.102
2 R. Cselkó, R. A. Pózmán, and L. Székely: Proc. 2023 IEEE Electrical Insulation Conf. (IEEE, 2023) pp. 1–4. https://doi.org/10.1109/EIC55835.2023.10177324
3 K. Chen, W. Chou, L. Liu, Y. Cui, P. Xue, and M. Jia: Sensors **19** (2019) 3676. https://doi.org/10.3390/s19173676
4 G. H. Kim: J. Polym. Sci. B Polym. Phys. **44** (2006) 1426. https://doi.org/10.1002/polb.20814
5 M. Sivan, D. Madheswaran, S. Hauzerova, V. Novotny, V. Hedvicakova, V. Jencova, E. K. Kostakova, M. Schindler, and D. Lukas: Mater. Today Chem. **26** (2022) 101025. https://doi.org/10.1016/j.mtchem.2022.101025
6 G. C. Rutledge and S. V. Fridrikh: Adv. Drug Deliv. Rev. **59** (2007) 1384. https://doi.org/10.1016/j.addr.2007.04.020
7 D. Sun, C. Chang, S. Li, and L. Lin: Nano Lett. **6** (2006) 839. https://doi.org/10.1021/nl0602701
8 G. Zheng, W. Li, X. Wang, D. Wu, D. Sun, and L. Lin: J. Phys. D: Appl. Phys. **43** (2010) 415501. https://doi.org/10.1088/0022-3727/43/41/415501
9 W.-H. Han, M.-Q. Wang, J.-X. Yuan, C.-C. Hao, C.-J. Li, Y.-Z. Long, and S. Ramakrishna: Arab. J. Chem. **15** (2022) 104193. https://doi.org/10.1016/j.arabjc.2022.104193
10 M. C. Lee, G. Y. Lin, Z. Y. Hoe, and C. T. Pan: Sensors **22** (2022) 9131. https://doi.org/10.3390/s22239131
11 M.-C. Lee, C.-T. Pan, S.-Y. Juan, Z.-H. Wen, J.-H. Xu, U. G. S. Janesha, and F.-M. Lin: Micromachines **15** (2024) 1213. https://doi.org/10.3390/mi15101213
12 X. You, C. Ye, and P. Guo: J. Manuf. Processes **30** (2017) 431. https://doi.org/10.1016/j.jmapro.2017.10.005
13 X.-X. He, J. Zheng, G.-F. Yu, M.-H. You, M. Yu, X. Ning, and Y.-Z. Long: J. Phys. Chem. C **121** (2017) 8663. https://doi.org/10.1021/acs.jpcc.6b12783
14 M. M. Nazemi, A. Khodabandeh, and A. Hadjizadeh: ACS Appl. Bio. Mater. **5** (2022) 394. https://doi.org/10.1021/acsabm.1c00944
15 G. Chen, G. Chen, L. Pan, and D. Chen: Diam. Relat. Mater. **129** (2022) 109358. https://doi.org/10.1016/j.diamond.2022.109358
16 J. Zhang, K. Guo, J. Guo, M. A. Newton, T. Li, and B. Xin: Polymer **316** (2025) 127815. https://doi.org/10.1016/j.polymer.2024.127815
17 M. M. Abolhasani, K. Shirvanimoghaddam, and M. Naebe: Compos. Sci. Technol. **138** (2017) 49. https://doi.org/10.1016/j.compscitech.2016.11.017
18 H. He, Y. Wang, B. Farkas, Z. K. Nagy, and K. Molnar: Mater. Des. **194** (2020) 108902. https://doi.org/10.1016/j.matdes.2020.108902
19 Y. R. Wang, J. M. Zheng, G. Y. Ren, and P. H. Zhang: Smart Mater. Struct. **20** (2011) 045009. https://doi.org/10.1088/0964-1726/20/4/045009
20 F. Xu, J. Yang, R. Dong, H. Jiang, C. Wang, W. Liu, Z. Jiang, X. Zhang, and G. Zhu: Adv. Fiber Mater. **3** (2021) 368. https://doi.org/10.1007/s42765-021-00095-7
21 S. Duan, J. Wu, J. Xia, and W. Lei: Sensors **20** (2020) 2820. https://doi.org/10.3390/s20102820